nanomaterials

MDPI

Article

Comprehensive Analysis of Temperature-Dependent Photoluminescence in Silica-Encapsulated $CsPbBr_3$ and $CsPbI_3$ Perovskite Nanocrystals

Ming Mei [1,†], Minju Kim [1,†], Sang Hyuk Park [2,†], Ga Eul Choi [1], Songyi Lee [3], Robert A. Taylor [4], Wei Chen [5], Suck Won Hong [1,*] and Kwangseuk Kyhm [1,*]

[1] Department of Cogno-Mechatronics Engineering, College of Nanoscience and Nanotechnology, Pusan National University, Busan 46241, Republic of Korea; mingmei@pusan.ac.kr (M.M.); minjukim108@pusan.ac.kr (M.K.); gecautumn@gmail.com (G.E.C.)
[2] Department of Life Sciences, Faculty of Natural Sciences, Imperial College London, London SW7 2AZ, UK; sanghyuk.park@imperial.ac.uk
[3] Department of Chemistry, Pukyong National University, Busan 48513, Republic of Korea; slee@pknu.ac.kr
[4] Department of Physics, University of Oxford, Oxford OX1 3PU, UK; robert.taylor@physics.ox.ac.uk
[5] Center for Intense Laser Application Technology, College of Engineering Physics, Shenzhen Technology University, Shenzhen 518118, China; chenwei@sztu.edu.cn
* Correspondence: swhong@pusan.ac.kr (S.W.H.); kskyhm@pusan.ac.kr (K.K.); Tel.: +82-51-510-2728 (K.K.)
† These authors contributed equally to this work.

Abstract

The temperature-dependent photoluminescence of $CsPbBr_3/SiO_2$ and $CsPbI_3/SiO_2$ nanocrystals was investigated to understand the thermal stability of SiO_2 encapsulation. At increased temperature, intensity quenching, linewidth broadening, energy level shift, and decay dynamics were evaluated as quantified parameters. Comprehensive analysis of these parameters supports that $CsPbI_3/SiO_2$ nanocrystals show a stronger interaction with phonons compared with $CsPbBr_3/SiO_2$ nanocrystals. Despite SiO_2 encapsulation, we conclude that trapping states are still present and the degree of localization can be characterized in terms of short-lived decay time and thermal activation energy.

Keywords: perovskite nanocrystal; stability; temperature dependence; band gap shift; thermal lattice expansion; electron–phonon interaction; non-radiative process

1. Introduction

Lead halide perovskites have emerged as promising, high-performance semiconductor materials for optoelectronic applications such as solar cells [1–3], photodetectors [3–5], light-emitting diodes (LEDs) [3,6,7], lasers [8–10], and photocatalysts [11,12]. Because of their remarkable properties, including high photoluminescence (PL) quantum yield, narrow emission linewidth, long carrier diffusion length, and tunable band gap, they have been widely investigated for next-generation device applications. In particular, all inorganic $CsPbX_3$ perovskites ($X = Cl^-, Br^-, I^-$) have attracted considerable interest in recent years due to their robust thermal stability compared to their hybrid organic–inorganic counterparts [3,5,7]. However, $CsPbX_3$ nanocrystals (NCs) still show structural, interfacial, and environmental degradation due to their soft ionic lattices and strong interactions with moisture and polar solvents [3,13,14]. In order to solve these problems, considerable effort has been devoted to improving stability such as compositional or surface engineering, matrix, and device encapsulation. In particular, the encapsulation of perovskite NCs with an

Academic Editor: Julian Maria Gonzalez Estevez

Received: 5 December 2025
Revised: 30 December 2025
Accepted: 30 December 2025
Published: 5 January 2026

appropriate inorganic protective layer such as SiO_2 [14–17], Cs_4PbBr_6 [18,19], Al_2O_3 [14,20], TiO_2 [21,22], and ZrO_2 [23,24] has been a highly effective and straightforward strategy for improving their stability. Among them, SiO_2 coating is particularly advantageous due to its excellent barrier properties against moisture and oxygen, which are the main causes of perovskite degradation. Moreover, its optical transparency across the visible spectrum ensures that they are less vulnerable to photo-degradation, making it highly suitable for optoelectronic applications [14,16,17].

For light harvesting applications, one of the most crucial optoelectronic properties of lead halide perovskite is their optical band gap. It is well known that the direct band gap of perovskites exhibits an atypical temperature dependence [25–27]. The conduction band minimum (CBM) of perovskites lies in the hybridized anti-bonding orbitals of the Pb 6*p* orbitals and the outer p orbitals of halide (5*p* for I, 4*p* for Br, and 3*p* for Cl), and the valence band maximum (VBM) lies in the hybridized anti-bonding states of the Pb 6*s* orbitals and the same halide *p*-orbital as that for the CBM. Regarding these electronic structures, the temperature-dependent band gap shift of perovskites is explained in terms of electron–phonon interactions in the corner-sharing $[PbX6]^{4-}$ octahedra [28] as well as thermal expansion.

Temperature dependence in single-crystal hybrid perovskites is also considered a crucial issue for inverse temperature crystallization and device applications [29–31]. Beyond encapsulation strategies for nanocrystals and polycrystalline films, single-crystal perovskites have emerged as a particularly promising materials for enhanced stability and reproducibility because the absence or high reduction of grain boundaries can suppress defect-assisted degradation mechanisms and ion-migration-related instabilities. Rapid growth routes, such as inverse temperature crystallization [29], have enabled high-quality bulk single crystals with markedly improved optoelectronic quality, motivating stability-oriented device concepts based on single-crystalline forms. More recently, low-dimensional single-crystal perovskites (i.e., 2D single-crystal hybrids) have also been actively investigated, leveraging their ordered quantum-well-like structures and improved environmental tolerance [30]. Thus, the stabilizat/ion of perovskite NCs via inorganic encapsulants can be considered a complementary approach that traces the dominant surface-mediated degradation channels specific to nanoscale systems [31].

Despite the great deal of work on SiO_2-coated $CsPbX_3$ perovskite NCs [32–35], their temperature dependence of the PL spectrum has rarely been addressed [36,37]. Among the $CsPbX_3$ perovskite family, most of the work has focused on green $CsPbBr_3$ due to the outstanding quantum yield and thermal stability, and recent work has analyzed the PL spectrum of $CsPbBr_3/SiO_2$ NCs for increasing temperature [36]. However, the quantified parameters were not compared with other $CsPbX_3$ perovskites. The quenching effect of $CsPbI_3/SiO_2$ NCs was observed in a limited temperature range ($25 \sim 253\,^{\circ}C$), and only intensity suppression was discussed [38,39]. The PL spectrum of $CsPbI_3/SiO_2$ NCs has never been analyzed at low temperatures, and the decay dynamics remain unknown.

In this work, we investigated the temperature-dependent PL spectrum of as-prepared $CsPbBr_3/SiO_2$ NCs and $CsPbI_3/SiO_2$ NCs, which both show enhanced stability compared with the uncoated bare NCs. As the temperature increased from 4 K to 300 K, the PL spectrum was interpreted comprehensively by comparing intensity quenching, linewidth broadening, energy level shift, and decay dynamics with quantified parameters. These results enabled us to evaluate the trapped states, and the atypical temperature dependence was explained via thermal exciton dissociation, lattice expansion, and exciton–phonon interaction.

2. Experimental Section

2.1. Material Preparation and Synthesis

We used the commercial products of Cesium carbonate (Cs_2CO_3, reagent Plus, 99%), 1-octadecene (ODE, technical grade, 90%), oleic acid (OA, technical grade, 90%), oleylamine (OAm, technical grade, 70%), toluene (anhydrous, 99.8%), (3-aminopropyl)triethoxysilane (APTES, 99%), lead iodide (PbI_2, 99%), methyl acetate (MeAc, reagent Plus, 99%), and ethyl acetate (EtAc, ACS reagent, ≥99.5%) from SigmaAldrich (Schnelldorf, Germany) , and lead bromide ($PbBr_2$, 99.998% metals basis) from Alfa Aesar (Shanghai, China). All chemicals were used as purchased without further purification.

The Cs-oleate precursor was prepared by dissolving Cs_2CO_3 (0.18 g) and oleic acid (0.75 mL) in 1-octadesene (7.5 mL). The mixture was stirred under vacuum and degassed at 120 °C for 1 h until a clear solution was obtained. For the synthesis of $CsPbBr_3$ NCs, $PbBr_2$ (0.07 g), oleic acid (0.5 mL), and oleylamine (0.5 mL) were dissolved in 1-octadescene (10 mL) and degassed at 120 °C for 40 min. The reaction flask was then filled with nitrogen, and the temperature was increased to 150 °C. Subsequently, 0.5 mL of the as-prepared Cs-oleaste solution was rapidly injected. After injection, the reaction mixture was immediately quenched via cooling in an ice-water bath. $CsPbBr_3/SiO_2$ NCs were synthesized using the same procedure as that for $CsPbBr_3$ NCs, except that APTES were used to substitute oleylamine. For the synthesis of $CsPbI_3$ NCs, PbI_2 (0.087 g), oleic acid (1 mL), oleylamine (1 mL), and 1-octadecene (10 mL) were added to a three-neck flask and degassed under vacuum at 100 °C for 50 min. The temperature was then raised to 140 °C under a nitrogen atmosphere, followed by the rapid injection of 0.5 mL of the Cs-oleate solution. The reaction was terminated by cooling the flask in an ice-water bath. $CsPbI_3/SiO_2$ NCs were prepared following the same procedure as that for $CsPbI_3$ NCs, with APTES substituted for oleylamine.

2.2. Characterization

UV-Vis absorption spectra were measured using a Spectramax M5 Microplate reader (Molecular Devices, Sunnyvale, CA, USA). Transmission electron microscopy (TEM), high-resolution transmission electron microscopy (HRTEM), and energy-dispersive X-ray spectrometry (EDS) compositional mapping images were also taken using a field emission transmission electron microscope (FETEM) operated at an accelerating voltage of 200 kV. Fourier transform infrared (FTIR) spectra were obtained. The temperature-dependent PL spectrum was obtained usinga closed-cycled cryostat (CCR), and time-resolved PL (TRPL) decay profiles were obtained using a time-correlated single photon counting (TCSPC) system with an instrument response function (IRF) of pulsed excitation (30 ps).

3. Results and Discussion

Figure 1a shows the three main processes involved in synthesizing $CsPbBr_3/SiO_2$ nanocrystals (NCs). Monodisperse $CsPbBr_3/SiO_2$ NCs are prepared using a modified one-pot hot-injection approach, where (3-aminopropyl) triethoxysilane (APTES) is used as a substitution for oleylamine (OAm) and acted as the capping agent and SiO_2 shell precursor [15,32,34]. With this method, the Cs-oleate precursor solution was quickly injected into a preheated mixture of $PbBr_2$, oleic acid (OA), APTES, and 1-octadecene (ODE) at 150 °C in a three-neck flask. Upon injection, $CsPbBr_3$ NCs nucleate and grow rapidly in solution. The reaction mixture is rapidly cooled to room temperature in order to stop further crystal growth and stabilize the NCs using an ice-water bath. For purification, the reaction mixture was washed with methyl acetate (MeAc), facilitating the interaction between APTES and the surface of the perovskite nanocrystals. Following this step, APTES underwent hydrolysis in the presence of moisture, where its ethoxy (-$SiOC_2H_5$) groups

hydrolyzed into silanol (-SiOH) groups. Then, SiOH reacted with $SiOC_2H_5$ and/or other SiOH to form Si-O-Si cross-linked networks. This process resulted in the encapsulation of the NCs within a protective silica matrix, which enhanced their stability against environmental degradation [34]. For the synthesis of $CsPbI_3/SiO_2$ NCs, we followed a similar procedure with PbI_2 substituting $PbBr_2$. Minor variations, such as synthesis temperature and the number of APTES, were previously mentioned in the Section 2.

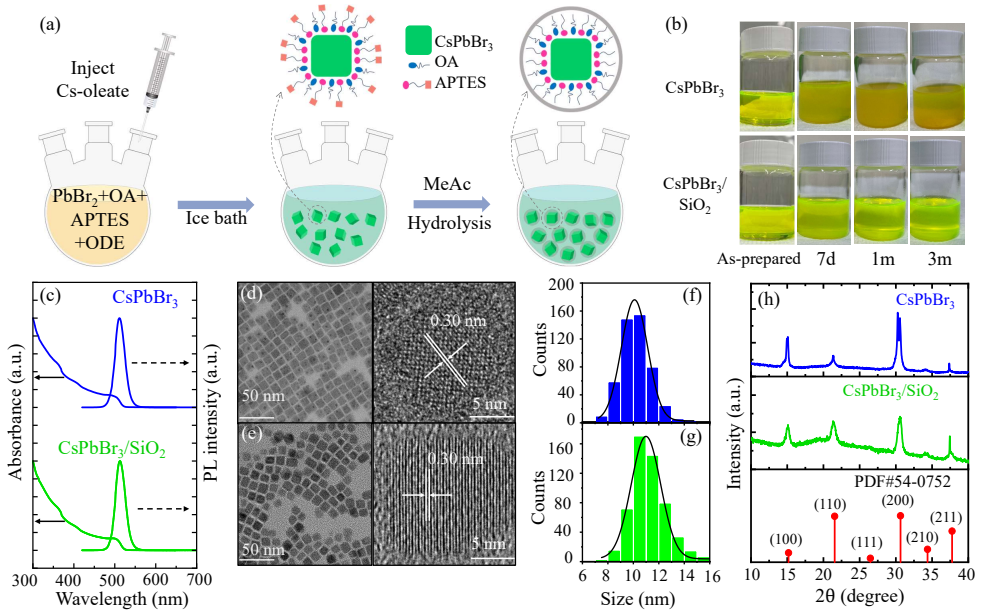

Figure 1. (**a**) Schematic of the synthesis process of $CsPbBr_3/SiO_2$ NCs. (**b**) As-prepared $CsPbBr_3$ and $CsPbBr_3/SiO_2$ toluene solution under day light following preservation in a refrigerator at 4 °C for 0 days, 7 days, 30 days (1 month), and 3 months. (**c**) PL and absorption spectrum of CsPbBr3 and $CsPbBr_3/SiO_2$. Transmission electron microscopy (TEM) images of $CsPbBr_3$ NCs (**d**) and $CsPbBr_3/SiO_2$ NCs (**e**), and the corresponding high-resolution transmission electron microscopy (HRTEM) images are also shown. (**g**) The size distribution histograms of $CsPbBr_3$ NCs (**f**) and $CsPbBr_3/SiO_2$ NCs. (**h**) X-ray diffraction (XRD) patterns of $CsPbBr_3$ (blue) and $CsPbBr_3/SiO_2$ NCs (green) compared with the standard pattern for cubic $CsPbBr_3$ (PDF#54-0752).

As shown in Figure 1b, photographs of $CsPbBr_3$ and $CsPbBr_3/SiO_2$ NC solutions in toluene were taken to monitor their degradation over time. Both of the NC solutions were stored in a refrigerator at 4 °C. It is evident that both fresh perovskite solutions were transparent with a yellow-green color. However, after 7 days, the $CsPbBr_3$ NC solution became opaque with significant aggregation. In contrast, the $CsPbBr_3/SiO_2$ solution remained transparent. Furthermore, after 30 days (1 month) and 3 months, the $CsPbBr_3/SiO_2$ solution was still transparent, while the $CsPbBr_3$ solution continued to aggregate over time. The improved stability of $CsPbBr_3/SiO_2$ NCs can be attributed to the presence of the SiO_2 shell, which passivates the perovskite NCs from the surface dangling bonds [16]. As a result, aggregation is suppressed, and solution stability is maintained over a long period.

Figure 1c shows the PL and absorption spectra of $CsPbBr_3$ NCs and $CsPbBr_3/SiO_2$ NCs, where the central PL wavelengths and linewidth (FWHM) of $CsPbBr_3/SiO_2$ NCs and $CsPbBr_3$ NCs are observed to be 513 nm/511 nm and 28.4 nm/27.8 nm, respectively. A uniform size distribution was observed in both TEM images of $CsPbBr_3$ NCs (Figure 1d) and $CsPbBr_3/SiO_2$ NCs (Figure 1e), and the HRTEM images also show a clear lattice spacing of 0.30 nm, which corresponds to the (200) plane of cubic-phase $CsPbBr_3$ [40]. These results indicate that the crystal integrity of $CsPbBr_3$ NCs is well preserved after silica coating. Because the shapes of both $CsPbBr_3$ NCs and $CsPbBr_3/SiO_2$ NCs are rectangular rather than square, the diagonal length of the rectangles was measured to determine the

size distribution. In Figure 1f and Figure 1g, the diagonal size distribution histograms of $CsPbBr_3$ NCs (10.2 ± 1.1 nm) and $CsPbBr_3/SiO_2$ NCs (11.3 ± 1.4 nm) are shown, respectively. Recent work observed a slight size expansion when $CsPbBr_3$ NCs are coated with SiO_2 [36,37]. Although the increased size causes a redshift as a result of the decreased confinement energy, the energy difference between $CsPbBr_3$ NCs and $CsPbBr_3/SiO_2$ NCs is barely seen.

To confirm the crystal structure of $CsPbBr_3$ NCs and $CsPbBr_3/SiO_2$ NCs, their X-ray diffraction (XRD) patterns were analyzed and compared with the standard PDF card, as shown in Figure 1h. The $CsPbBr_3/SiO_2$ NCs exhibit strong diffraction peaks at 2θ = 15.2°, 21.5°, 30.8°, 34.5°, and 37.8°, corresponding to the planes of (100), (110), (200), (210), and (211) in cubic $CsPbBr_3$ (PDF#54-0752) [35], respectively. It is also noticeable that no structural phase transition was observed after silica shell coating, and this result indicates that the crystal integrity of $CsPbBr_3$ NCs was well preserved. These XRD results are consistent with the high-resolution TEM images shown in the insets of Figure 1d,e, which confirm the structural stability of the $CsPbBr_3/SiO_2$ NCs. Although the diffracted peak intensity of $CsPbBr_3/SiO_2$ NCs appears decreased compared with that of bare $CsPbBr_3$ NCs, this is mainly attributed to the incorporation of an amorphous SiO_2 fraction, which dilutes the crystalline perovskite content and increases diffuse background scattering. It is important that the unchanged peak positions and the absence of additional reflections confirm that the cubic $CsPbBr_3$ crystal phase was preserved after encapsulation.

The atomic-resolution scanning transmission electron microscopy (STEM) images, which were acquired in a high-angle annular dark field (HAADF) mode (Figure S1 in the Supplementary Materials), revealed that $CsPbBr_3$ NCs were embedded within the silica shell. Additionally, the soft edges observed in the TEM images of $CsPbBr_3/SiO_2$ NCs further indicated the presence of an ultrathin SiO_2 shell [26]. The Fourier transform infrared (FTIR) spectrum (Figure S2 in the Supplementary Materials) provided additional evidence for the core–shell structure of $CsPbBr_3/SiO_2$ NCs. The sharp peak at approximately 1128 cm^{-1} was attributed to the stretching vibration of the Si–O–Si bond [26]. Moreover, the peak at around 1033 cm^{-1} corresponded to the vibration of the Si–O–C bond. The detected peaks at approximately 2854 cm^{-1} and 2923 cm^{-1} were assigned to the asymmetric and symmetric stretching vibrations of C–H, respectively.

As demonstrated in the case of $CsPbBr_3$, SiO_2 encapsulation contributed to improved stability. Given these promising results, $CsPbI_3$ NCs were also encapsulated with SiO_2 to examine whether a similar stabilization effect could be achieved. It is known that the ammonium ligands of $CsPbI_3$ NCs are easily lost due to the weak acid–base interactions between I and oleylammonium, resulting in fast agglomeration and an undesired phase transformation from cubic to orthorhombic. Their thermodynamically unstable α-phase also causes rapid degradation. To revolve these unstable issues in $CsPbI_3$ NCs, many strategies were known to improve its stability such as introducing organolead compound trioctylpho sphine-PbI_2 (TOP-PbI_2) as the reactive precursor [41], utilizing ZnI_2 as a co-precursor and passivating agent in the synthesis [42].

As shown in Figure 2a, two solutions were prepared: a brown-colored $CsPbI_3/SiO_2$ NC solution and a burgundy-colored pristine $CsPbI_3$ NC solution. To remove excess ligands and byproducts from the reaction, both solutions underwent a purification step using methyl acetate. During this process, the pristine $CsPbI_3$ NC solution was found to show rapid degradation and changed color from burgundy to white, indicating structural instability. In contrast, the $CsPbI_3/SiO_2$ NC solution retained its original brown color, demonstrating that the SiO_2 shell effectively prevented degradation (Figure S6 in the Supplementary Materials). However, $CsPbI_3$ NCs exhibited a distinct behavior compared to

$CsPbBr_3$ NCs, undergoing rapid PL quenching upon purification. This inhibits comparative studies on their optical properties.

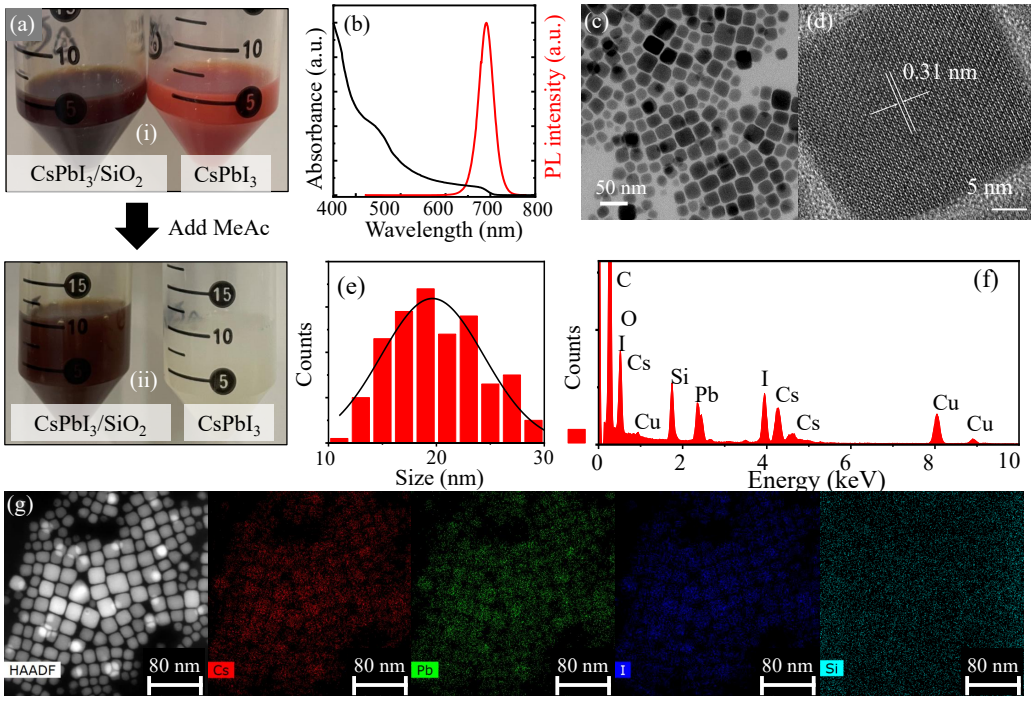

Figure 2. (**a**) A total of 5 mL of as-prepared $CsPbI_3$ and $CsPbI_3/SiO_2$ pristine solution (**i**), and the two pristine perovskite solution after adding 5 mL methyl acetate into 5 mL (**ii**), where the insets are photographs of $CsPbI_3/SiO_2$ toluene solution under day light, respectively. (**b**) PL and absorption spectra of $CsPbI_3/SiO_2$ NCs. Given TEM (**c**) and HRTEM (**d**) images of $CsPbI_3/SiO_2$ NCs, the size distribution histogram was obtained (**e**) as well as the lattice spacing. (**f**) The energy-dispersive X-ray (EDX) spectrum of $CsPbI_3/SiO_2$ NCs. (**g**) For an STEM-HAADF image of $CsPbI_3/SiO_2$ NCs, the elemental mapping images of Cs, Pb, I, and Si were compared.

The stability of $CsPbI_3/SiO_2$ NCs was further confirmed, as no noticeable quenching was observed over time. To investigate their optical properties, the absorption and PL spectra of $CsPbI_3/SiO_2$ NCs were measured as shown in Figure 2b. The absorption spectrum exhibited two prominent peaks near 680 nm and 450 nm. The PL spectrum showed a peak centered around 690 nm with a full width at half maximum (FWHM) of 39 nm, which is broader than that of $CsPbBr_3/SiO_2$ NCs (28.4 nm). The relatively narrow FWHM value also indicates a uniform size distribution of $CsPbI_3/SiO_2$ NCs. This observation was further supported by the TEM image in Figure 2c, which visually confirms the uniform morphology of the nanocrystals. The HRTEM image in Figure 2d also shows clear lattice fringes of $CsPbI_3/SiO_2$ NCs, indicating their high crystalline quality. The measured lattice spacing distance of 0.31 nm corresponds to the (200) planes of cubic-phase $CsPbI_3$, further confirming the structural integrity of the encapsulated NCs. The corresponding size distribution analysis reveals that the $CsPbI_3/SiO_2$ NCs have an average size of approximately 20.3 nm with a standard deviation of $\pm$4.4 nm, as shown in Figure 2e.

Figure 2f shows the energy-dispersive X-ray (EDX) spectrum of $CsPbI_3/SiO_2$ NCs, while Figure 2g displays the STEM-HAADF image and elemental mapping images, confirming the successful formation of the silica shell around $CsPbI_3/SiO_2$ NCs. For further verification of a core–shell structure, Fourier transform infrared (FTIR) spectroscopy was performed (Figure S2 in Supplementary Materials), revealing strong peaks at 1037 cm^{-1} and 1070 cm^{-1}, which correspond to the stretching vibrations of Si-O-Si [39] and Si-O-C [43] bonds, respectively. To assess the effect of the silica shell on the crystal structure of

$CsPbI_3/SiO_2$ NCs, X-ray diffraction (XRD) measurements were conducted and compared with the reference pattern from ICSD no. 181288 (Figure S4 in the Supplementary Materials). The XRD peaks of $CsPbI_3/SiO_2$ NCs closely match those of ICSD no. 181288 within the range of $2\theta = 10°–40°$, confirming that $CsPbI_3/SiO_2$ NCs retain a cubic phase.

Although the temperature-dependent PL spectrum in perovskites NCs was extensively investigated [25–28,36–38], a systematic study of the core–shell perovskite NCs is still necessary. In Figure 3a and 3b, the PL intensity of $CsPbBr_3/SiO_2$ NCs and $CsPbI_3/SiO_2$ NCs was obtained for spectrum and temperature, respectively. The integrated PL intensity of $CsPbBr_3/SiO_2$ NCs (Figure 3c) and $CsPbI_3/SiO_2$ NCs (Figure 3d) is also shown for reciprocal temperature ($1000/T$) to evaluate thermal activation. With increasing temperature, thermally activated non-radiative recombination processes, leading to a gradual decrease in PL intensity. For quantitative evaluation, a model with the Arrhenius equation was utilized [26]:

$$I(T) = \frac{I_0}{1 + A\exp(-\frac{E_A}{k_B T})} \quad (1)$$

where $I(T)$ and I_0 are the integrated PL intensity at temperature T and 0 K, respectively. Regarding the relative intensity quenching with $I_0/I(T) = 1 + A\exp(-E_A/k_B T)$, it is plausible that an activation energy E_A in the Boltzmann factor can be obtained with a fitting constant A, which is associated with thermal dissociation. In the case of $CsPbI_3/SiO_2$, a high $E_A = 63.8 \pm 11.9$ meV was obtained, which is comparable to its exciton binding energy. This result suggests that thermal exciton dissociation is a dominant mechanism of PL quenching. Moreover, a low $E_A = 14.9 \pm 1.5$ meV was obtained in $CsPbBr_3/SiO_2$ NCs. Therefore, the presence of additional non-radiative processes is expected, such as trap-assisted carrier recombination, exciton delocalization, and phonon-mediated scattering. Hence, $CsPbBr_3/SiO_2$ NCs are vulnerable to non-radiative losses, and this may explain the significant difference between Figure 3a,b.

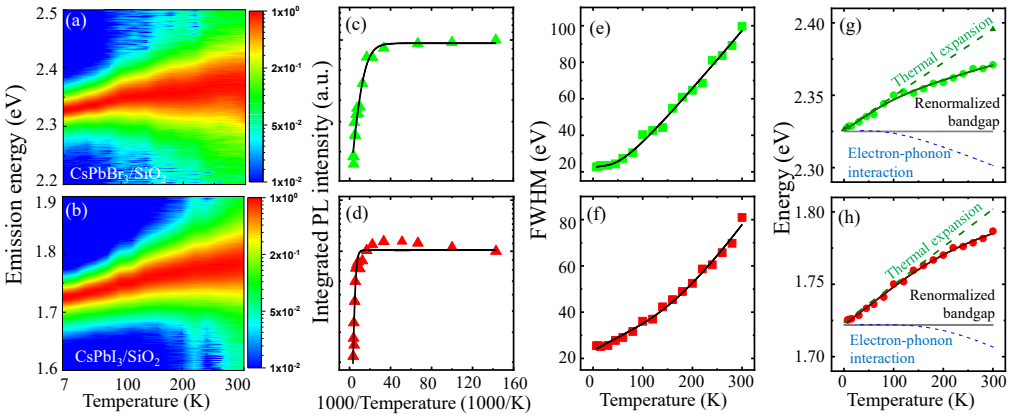

Figure 3. (**a**,**b**) Given the temperature-dependent PL spectrum of $CsPbBr_3/SiO_2$ and $CsPbI_3/SiO_2$ NCs, which are normalized to the peak intensity for clarity, spectrally integrated PL intensity (**c**,**d**), linewidth (**e**,**f**), and peak energy (**g**,**h**) are plotted with regard to temperature, respectively.

Enhanced phonon scattering for temperature leads to a linewidth broadening of the PL spectrum, and this can be described by the following equation [25,26]:

$$\Gamma(T) = \Gamma_0 + \sigma T + \frac{\Gamma_{op}}{\exp(E_{op}/k_B T) - 1} \quad (2)$$

where Γ_0 is the inhomogeneous linewidth independent of temperature, caused by variations in the size, shape, and composition of NCs. The linear term (σT) is attributed to the acoustic–phonon interaction with the acoustic–phonon coupling coefficients (σ). The third nonlinear

term is described in terms of the coupling coefficient (Γ_{op}) and the energy (E_{op}) of optical phonons, which are associated with the Bose–Einstein distribution.

In Figure 3e,f, the temperature-dependent linewidth of $CsPbBr_3/SiO_2$ NCs and $CsPbI_3/SiO_2$ NCs is fitted with Equation (2), where the fitting parameters are summarized in Table S1 of the Supplementary Materials. With increasing temperature from 7 K to 300 K, the linewidth becomes broadened by 76.96 meV and 55.43 meV in $CsPbBr_3/SiO_2$ NCs and $CsPbI_3/SiO_2$ NCs, respectively. The inhomogeneous linewidths of $CsPbBr_3/SiO_2$ ($\Gamma_0 = 22.48 \pm 1.91$ meV) and $CsPbI_3/SiO_2$ ($\Gamma_0 = 23.41 \pm 0.927$ meV) are significantly narrow compared to the recent results of uncoated $CsPbBr_3$ NCs (40.04 ± 0.45 meV) and $CsPbI_3$ NCs (52.12 ± 0.71 meV). This result indicates that the size homogeneity and surface passivation are improved in $CsPbBr_3/SiO_2$ NCs and $CsPbI_3/SiO_2$ NCs. We found that the optical phonon interaction of the third term is dominant compared with the acoustic interaction of the second term ($\sim \sigma T$), and the E_{LO} of $CsPbBr_3/SiO_2$ (15.516 ± 6.102 meV) and $CsPbI_3/SiO_2$ (55.106 ± 17.151 meV) were comparable to the LO phonon energy [36].

As temperature increases, the band gap shift can be observed. The renormalized band gap $E_g(T)$ can be described by the following equation [25,27]:

$$E_g(T) = E_0 + A_T T + A_P \left[\frac{2}{\exp(E_P/k_B T) - 1} + 1 \right] \quad (3)$$

where the thermal lattice expansion effect results in a linear dependence for temperature ($\sim A_T T$) with the thermal expansion coefficient A_T, and the electron–phonon interaction of the third term leads to a nonlinear temperature dependence with the phonon coupling strength $A_P < 0$ and the average optical phonon energy E_P. Given the band gap E_0 at $T = 0$ K, the thermal lattice expansion effect causes a blueshift of the band gap, but the electron–phonon interaction gives rise to an opposite redshift. Given the PL peak energy of $CsPbBr_3/SiO_2$ NCs (Figure 3g) and $CsPbI_3/SiO_2$ NCs (Figure 3h), Equation (3) was fitted (solid line), and the parameters are shown in Table S2 of the Supplementary Materials. This model enables us to separate the two effects of thermal lattice expansion and electron–phonon interaction (dotted lines). At low temperatures, the band gap shift is dominated by the thermal lattice expansion. In the case of typical semiconductors, the thermal lattice expansion results in a band gap decrease ($A_T < 0$). In contrast, we obtained positive A_T for $CsPbBr_3/SiO_2$ (0.23 ± 0.03 meV/K) and $CsPbI_3/SiO_2$ (0.26 ± 0.02 meV/K). In the case of perovskite ($CsPbX_3$) NCs, the anti-bonding nature of the interaction between Pb 6*s* and halide *p* orbitals becomes significant, and this leads to a distinctive thermal expansion effect of the $[PbX_6]^{4-}$ octahedral framework.

At high temperatures, sufficient thermal energy excites large energy phonon states, and the Bose–Einstein distribution in the third term of Equation (2) becomes significant due to the activated optical phonon modes. This effect was quantified in terms of the phonon coupling strength (A_P) and the average optical phonon energy (E_P). A large $A_P = 93.3$ meV was obtained in $CsPbI_3/SiO_2$ compared with the small $A_P = 25.3$ meV in $CsPbBr_3/SiO_2$. The large E_P in $CsPbI_3/SiO_2$ (66.6 meV) can also explain why the electron–phonon interaction effect remains suppressed at low temperatures. However, the small E_P in $CsPbBr_3/SiO_2$ (29.3 meV) provides a relatively lower temperature threshold to activate optical phonons.

In Figure 4, the time-resolved PL intensity of $CsPbBr_3/SiO_2$ NCs (a,c) and $CsPbI_3/SiO_2$ NCs (b,d) is plotted for temperature, which were selected at the dominant PL energy, respectively. For quantitative analysis, two kinds of decay times in $CsPbBr_3/SiO_2$ NCs

(Figure 4e,g) and $CsPbI_3/SiO_2$ NCs (Figure 4f,h) were obtained at various temperatures using a bi-exponential model,

$$E_g(T) = A_1 \exp(-t/\tau_1) + A_2 \exp(-t/\tau_2) \quad (4)$$

where τ_1 and τ_2 are the short- and long-lived decay time, and A_1 and A_2 are the corresponding amplitudes, respectively. For increasing temperature, we found that τ_1 barely changes with decreased A_1. However, both τ_2 and A_2 show a significant increase for temperature. These results are associated with thermally activated carriers and phonons. At low temperatures, excited carriers are initially trapped in localized states. However, thermal activation suppresses the non-radiative trapping. Exciton recombination time can also be elongated as the interaction with phonons becomes pronounced. While the former mechanism alters the relative weight of τ_1 and τ_2, the latter enhances the dark exciton states and the exciton dissociation. Recent work has reported a similar evidence in the strong exciton–phonon coupling in $CsPbX_3$ perovskite structures [44]. Interestingly, for increasing temperature from 7 K to 300 K, τ_2 of $CsPbBr_3/SiO_2$ NCs increases from 4 ns to 10 ns, but the change in τ_2 in $CsPbI_3/SiO_2$ NCs is more significant: 40 ns at 300 K. This result is also consistent with the high $A_P = 93.3$ meV of $CsPbI_3/SiO_2$ NCs compared with that of $CsPbBr_3/SiO_2$ NCs ($A_P = 25.3$ meV).

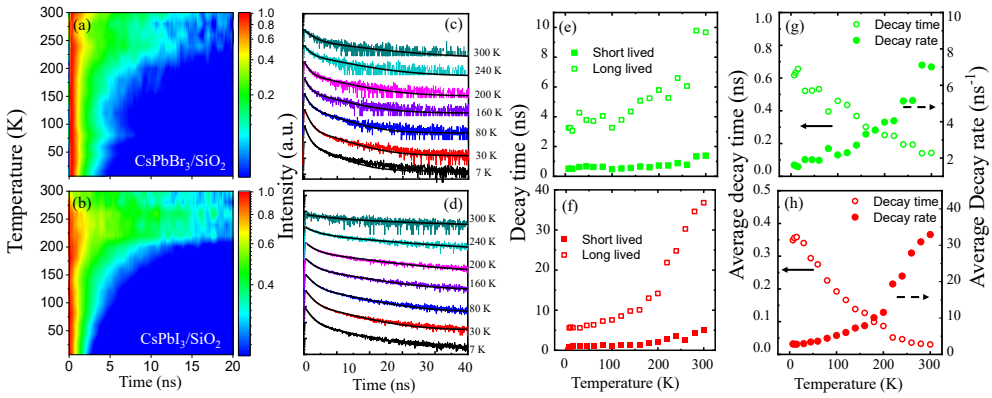

Figure 4. (**a**,**b**) Given time-resolved PL intensity of $CsPbBr_3/SiO_2$ and $CsPbI_3/SiO_2$ NCs for increasing temperature, the PL intensity decay were fitted by the bi-exponential model at various temperatures (**c**,**d**), respectively. This enables us to obtain short- and long-lived decay time for temperature (**e**,**f**), whereby the corresponding average decay time and average decay rate were also obtained for temperature (**g**,**h**).

To obtain a representative quantity of the decay feature, the average decay time (τ_{avg}) was also obtained using the four parameters in the bi-exponential model as

$$\tau_{avg} = \frac{A_1\tau_1^2 + A_2\tau_2^2}{A_1\tau_1 + A_2\tau_2}. \quad (5)$$

In Figure 4g,h, the τ_{avg} and $1/\tau_{avg}$ of $CsPbBr_3/SiO_2$ NCs and $CsPbI_3/SiO_2$ NCs are shown for increasing temperature, respectively. Compared with bare $CsPbBr_3$ NCs, $CsPbBr_3/SiO_2$ NCs are known to show a prolonged PL decay time [36]. The overall feature was correct, but the monotonic model was not enough to define a representative decay time. It is noticeable that the amplitudes (A_1 and A_2) were also considered to obtain the average decay time. At low temperatures, $1/\tau_{avg}$ shows a gradual increase, but a dramatic increase occurs at a critical temperature ($\tau_c \sim 200$ K). This critical phenomenon is significant in $CsPbI_3/SiO_2$ NCs and is consistent with the strong phonon interactions with the high A_P and E_P. Therefore, τ_c is useful to evaluate the degree of localization and thermal activation.

As an additional remark, $CsPbI_3$ /SiO_2 NCs can be an attractive material system for optical devices. In particular, they are suitable for LED and phosphor-converted color conversion, where their band gap tunability and narrow emission linewidths enable spectrally pure red emission for wide-color-gamut displays and high-brightness solid-state lighting. At the same time, these favorable optical characteristics are also useful in photodetector and photo-conductive architectures, in which strong absorption coefficients and well-defined band edges facilitate efficient photo-carrier generation. Nevertheless, these applications are constrained by temperature-activated non-radiative recombination pathways and phase instability, which are often exacerbated under operational conditions. In this context, it is important to understand how encapsulation-induced stabilization translates into temperature-resilient optical behavior.

4. Conclusions

Compared with the bare NCs of $CsPbBr_3$ and $CsPbI_3$, we confirmed that SiO_2 encapsulation improves the stability of the core–shell structures. Although the core crystal structures remain unaffected in the presence of a SiO_2 shell, we found that trapping states are still present. Their degree of localization can be quantified in terms of a short-lived decay time and thermal activation energy, as well as the vibration modes of the Si–O–Si and Si–O–C bonds. From our comprehensive analysis of the intensity, linewidth, energy level shift, and decay time of PL spectrum at increased temperature, we concluded that $CsPbI_3/SiO_2$ NCs show a stronger interaction with phonons compared with $CsPbBr_3/SiO_2$ NCs.

Supplementary Materials: The following supporting information can be downloaded at: https://www.mdpi.com/article/10.3390/nano16010076/s1, Figure S1: STEM-HAADF image for $CsPbBr_3/SiO_2$; Figure S2: FTIR spectrum; Figure S3: The as-prepared $CsPbBr_3$ and $CsPbBr_3/SiO_2$ toluene solution under day light; Figure S4: XRD pattern; Figure S5: The as-prepared $CsPbI_3$ and $CsPbI_3/SiO_2$ toluene solution; Figure S6: Visualization of RGB color evolution of $CsPbI_3$ and $CsPbI_3/SiO_2$ toluene solution; Table S1: Fitting parameters for PL FWHM; Table S2: Fitting parameters for PL peak energy.

Author Contributions: Conceptualization, S.W.H. and K.K.; methodology, M.M., G.E.C. and S.L.; software, M.K.; validation, M.K., M.M. and K.K.; formal analysis, M.K., M.M., and S.H.P.; investigation, M.M. and W.C.; resources, S.W.H.; data curation, M.M.; writing—original draft preparation, M.K., M.M. and K.K.; writing—review and editing, M.K., R.A.T. and K.K.; visualization, M.K.; supervision, K.K.; project administration, K.K.; funding acquisition, K.K. All authors have read and agreed to the published version of the manuscript.

Funding: This research was supported by the BrainLink program (RS-2023-00236798), funded by the Ministry of Science and ICT through the National Research Foundation of Korea, as well as by the Korean Government (MSIT) (No. 2022R1A5A8023404, RS-2025-25421510) and by the RISE program, funded by the Ministry of Education (MOE) and the Busan Metropolitan City (2025-RISE-02-004-202511980001-01).

Data Availability Statement: The data presented in this study are available on request from the corresponding author.

Conflicts of Interest: The authors declare no conflicts of interest.

References

1. Ma, Q.; Wang, Y.; Liu, L.; Yang, P.; He, W.; Zhang, X.; Zheng, J.; Ma, M.; Wan, M.; Yang, Y.; et al. One-step dual-additive passivated wide-bandgap perovskites to realize 44.72%-efficient indoor photovoltaics. *Energy Environ. Sci.* **2024**, *17*, 1637–1644. [CrossRef]
2. Liu, M.; Johnston, M.B.; Snaith, H.J. Efficient planar heterojunction perovskite solar cells by vapour deposition. *Nature* **2013**, *501*, 395–398. [CrossRef]
3. Pan, Y.; Zhang, Y.; Kang, W.; Deng, N.; Yan, Z.; Sun, W.; Kang, X.; Ni, J. Progress in the preparation and application of $CsPbX_3$ perovskites. *Mater. Adv.* **2022**, *3*, 4053–4068. [CrossRef]

4. Liu, Y.; Gong, W.; Xiang, F.; Li, Y.; Guo, H.; Hao, F.; Niu, X. High-Performance Self-Powered Photodetectors with Space-Confined Hybrid Lead Halide Perovskite Nanocrystals. *Adv. Opt. Mater.* **2022**, *11*, 2202215. [CrossRef]
5. Wang, S.; Wang, K.; Gu, Z.; Wang, Y.; Huang, C.; Yi, N.; Xiao, S.; Song, Q. Solution-Phase Synthesis of Cesium Lead Halide Perovskite Microrods for High-Quality Microlasers and Photodetectors. *Adv. Opt. Mater.* **2017**, *5*, 1700023. [CrossRef]
6. Lin, K.; Xing, J.; Quan, L.N.; de Arquer, F.P.G.; Gong, X.; Lu, J.; Xie, L.; Zhao, W.; Zhang, D.; Yan, C.; et al. Perovskite light-emitting diodes with external quantum efficiency exceeding 20 per cent. *Nature* **2018**, *562*, 245–248. [CrossRef]
7. Feng, W.; Lin, K.; Li, W.; Xiao, X.; Lu, J.; Yan, C.; Liu, X.; Xie, L.; Tian, C.; Wu, D.; et al. Efficient all-inorganic perovskite light-emitting diodes enabled by manipulating the crystal orientation. *J. Mater. Chem. A* **2021**, *9*, 11064–11072. [CrossRef]
8. Shaklee, K.L.; Leheny, R.F. Direct Determination of Optical Gain in Semiconductor Crystals. *Appl. Phys. Lett.* **1971**, *18*, 475–477. [CrossRef]
9. Tatarinov, D.A.; Anoshkin, S.S.; Tsibizov, I.A.; Sheremet, V.; Isik, F.; Zhizhchenko, A.Y.; Cherepakhin, A.B.; Kuchmizhak, A.A.; Pushkarev, A.P.; Demir, H.V.; et al. High-Quality $CsPbBr_3$ Perovskite Films with Modal Gain above 10 000 cm^{-1} at Room Temperature. *Adv. Opt. Mater.* **2023**, *11*, 2202407. [CrossRef]
10. Alvarado-Leaños, A.L.; Cortecchia, D.; Folpini, G.; Srimath Kandada, A.R.; Petrozza, A. Optical Gain of Lead Halide Perovskites Measured via the Variable Stripe Length Method: What We Can Learn and How to Avoid Pitfalls. *Adv. Opt. Mater.* **2021**, *9*, 2001773. [CrossRef]
11. Park, S.; Chang, W.J.; Lee, C.W.; Park, S.; Ahn, H.-Y.; Nam, K.T. Photocatalytic hydrogen generation from hydriodic acid using methylammonium lead iodide in dynamic equilibrium with aqueous solution. *Nat. Energy* **2016**, *2*, 16185. [CrossRef]
12. Xu, Y.F.; Yang, M.Z.; Chen, B.X.; Wang, X.D.; Chen, H.Y.; Kuang, D.B.; Su, C.Y. A $CsPbBr_3$ Perovskite Quantum Dot/Graphene Oxide Composite for Photocatalytic CO_2 Reduction. *J. Am. Chem. Soc.* **2017**, *139*, 5660–5663. [CrossRef]
13. Protesescu, L.; Yakunin, S.; Bodnarchuk, M.I.; Krieg, F.; Caputo, R.; Hendon, C.H.; Yang, R.X.; Walsh, A.; Kovalenko, M.V. Nanocrystals of Cesium Lead Halide Perovskites ($CsPbX_3$, X = Cl, Br, and I): Novel Optoelectronic Materials Showing Bright Emission with Wide Color Gamut. *Nano Lett.* **2015**, *15*, 3692–3696. [CrossRef] [PubMed]
14. Wei, Y.; Cheng, Z.; Lin, J. An overview on enhancing the stability of lead halide perovskite quantum dots and their applications in phosphor-converted LEDs. *Chem. Soc. Rev.* **2019**, *48*, 310–350. [CrossRef]
15. Sun, C.; Zhang, Y.; Ruan, C.; Yin, C.; Wang, X.; Wang, Y.; Yu, W.W. Efficient and Stable White LEDs with Silica-Coated Inorganic Perovskite Quantum Dots. *Adv. Mater.* **2016**, *28*, 10088–10094. [CrossRef]
16. Zhong, Q.; Cao, M.; Hu, H.; Yang, D.; Chen, M.; Li, P.; Wu, L.; Zhang, Q. One-Pot Synthesis of Highly Stable $CsPbBr_3$@SiO_2 Core-Shell Nanoparticles. *ACS Nano* **2018**, *12*, 8579–8587. [CrossRef] [PubMed]
17. Mei, M.; Han, Z.; Liu, P.; Fang, F.; Chen, W.; Hao, J.; Wu, D.; Pan, R.; Cao, W.; Wang, K. Silica encapsulation of metal perovskite nanocrystals in a photoluminescence type display application. *Nanotechnology* **2019**, *30*, 395702. [CrossRef]
18. Wang, C.; Yan, L.; Si, J.; Huo, T.; Hou, X. Strongly luminescent and highly stable $CsPbBr_3/Cs_4PbBr_6$ core/shell nanocrystals and their ultrafast carrier dynamics. *J. Alloys Compd.* **2023**, *946*, 169272. [CrossRef]
19. Chen, Y.M.; Zhou, Y.; Zhao, Q.; Zhang, J.Y.; Ma, J.P.; Xuan, T.T.; Guo, S.Q.; Yong, Z.J.; Wang, J.; Kuroiwa, Y.; et al. $Cs_4PbBr_6/CsPbBr_3$ Perovskite Composites with Near-Unity Luminescence Quantum Yield: Large-Scale Synthesis, Luminescence and Formation Mechanism, and White Light-Emitting Diode Application. *ACS Appl. Mater. Interfaces* **2018**, *10*, 15905–15912. [CrossRef]
20. Loiudice, A.; Saris, S.; Oveisi, E.; Alexander, D.T.L.; Buonsanti, R. $CsPbBr_3$ QD/AlO_x Inorganic Nanocomposites with Exceptional Stability in Water, Light, and Heat. *Angew. Chem. Int. Ed.* **2017**, *56*, 10696–10701. [CrossRef]
21. Li, Z.J.; Hofman, E.; Li, J.; Davis, A.H.; Tung, C.H.; Wu, L.Z.; Zheng, W. Photoelectrochemically Active and Environmentally Stable $CsPbBr_3/TiO_2$ Core/Shell Nanocrystals. *Adv. Funct. Mater.* **2017**, *28*, 1704288. [CrossRef]
22. Liu, W.; Liu, J.; Wang, X.; He, J.; Li, Y.; Liu, Y. Synthesis of Asymmetrical $CsPbBr_3/TiO_2$ Nanocrystals with Enhanced Stability and Photocatalytic Properties. *Catalysts* **2023**, *13*, 1048. [CrossRef]
23. Liu, H.; Tan, Y.; Cao, M.; Hu, H.; Wu, L.; Yu, X.; Wang, L.; Sun, B.; Zhang, Q. Fabricating $CsPbX_3$-Based Type I and Type II Heterostructures by Tuning the Halide Composition of Janus $CsPbX_3/ZrO_2$ Nanocrystals. *ACS Nano* **2019**, *13*, 5366–5374. [CrossRef] [PubMed]
24. Wang, K.; Yao, R.; Shen, P.; Fang, Y.; Chen, L.; Wang, H. Quantum Dots Encapsulated by ZrO_2 Enhance the Stability of Perovskite Solar Cells. *Adv. Mater. Interfaces* **2021**, *8*, 2100776. [CrossRef]
25. Wei, K.; Xu, Z.; Chen, R.; Zheng, X.; Cheng, X.; Jiang, T. Temperature-dependent excitonic photoluminescence excited by two-photon absorption in perovskite $CsPbBr_3$ quantum dots. *Opt. Lett.* **2016**, *41*, 3821–3824. [CrossRef]
26. Ai, B.; Liu, C.; Deng, Z.; Wang, J.; Han, J.; Zhao, X. Low temperature photoluminescence properties of $CsPbBr_3$ quantum dots embedded in glasses. *Phys. Chem. Chem. Phys.* **2017**, *19*, 17349–17355. [CrossRef] [PubMed]
27. Saran, R.; Heuer-Jungemann, A.; Kanaras, A.G.; Curry, R.J. Giant Bandgap Renormalization and Exciton–Phonon Scattering in Perovskite Nanocrystals. *Adv. Opt. Mater.* **2017**, *5*, 17000231. [CrossRef]

28. Xu, J.; Yu, S.; Shang, X.; Chen, X. Temperature Dependence of Bandgap in Lead-Halide Perovskites with Corner-Sharing Octahedra. *Adv. Photonics Res.* **2022**, *4*, 2200193. [CrossRef]
29. Saidaminov, M.I.; Abdelhady, A.L.; Murali, B.; Alarousu, E.; Burlakov, V.M.; Peng, W.; Dursun, I.; Wang, L.; He, Y.; Maculan, G.; et al. High-quality bulk hybrid perovskite single crystals within minutes by inverse temperature crystallization. *Nat. Commun.* **2015**, *6*, 7586. [CrossRef]
30. Demontis, V.; Durante, O.; Marongiu, D.; De Stefano, S.; Matt, S.; Simbula, A.; Capello, C.R.; Pennelli, G.; Quochi, F.; Saba, M.; et al. Photoconduction in 2D Single-Crystal Hybrid Perovskites. *Adv. Opt. Mater.* **2025**, *13*, 2402469. [CrossRef]
31. Bttula, R.K.; Sudakar, C.; Bhyrappa, P.; Veerappan, G.; Ramasamy, E. Single-Crystal Hybrid Lead Halide Perovskites: Growth, Properties, and Device Integration for Solar Cell Application. *Cryst. Growth Des.* **2022**, *10*, 6338–6362. [CrossRef]
32. Zhao, H.; Wei, L.; Zeng, P.; Liu, M. Formation of highly uniform thinly-wrapped $CsPbX_3$@silicone nanocrystals via self-hydrolysis: Suppressed anion exchange and superior stability in polar solvents. *J. Mater. Chem. C* **2019**, *7*, 9813–9819. [CrossRef]
33. Song, W.; Wang, Y.; Wang, B.; Yao, Y.; Wang, W.; Wu, J.; Shen, Q.; Luo, W.; Zou, Z. Super stable $CsPbBr_3$@SiO_2 tumor imaging reagent by stress-response encapsulation. *Nano Res.* **2020**, *13*, 795–801. [CrossRef]
34. Trinh, C.K.; Lee, H.; So, M.G.; Lee, C.L. Synthesis of Chemically Stable Ultrathin SiO_2-Coated Core-Shell Perovskite QDs via Modulation of Ligand Binding Energy for All-Solution-Processed Light-Emitting Diodes. *ACS Appl. Mater. Interfaces* **2021**, *13*, 29798–29808. [CrossRef] [PubMed]
35. Gao, F.; Yang, W.; Liu, X.; Li, Y.; Liu, W.; Xu, H.; Liu, Y. Highly stable and luminescent silica-coated perovskite quantum dots at nanoscale-particle level via nonpolar solvent synthesis. *Chem. Eng. J.* **2021**, *407*, 128001. [CrossRef]
36. Zhang, C.; Zhang, H.; Wang, R.; You, D.; Wang, W.; Xu, C.; Dai, J. Exciton photoluminescence of $CsPbBr_3$@SiO_2 quantum dots and its application as a phosphor material in light-emitting devices. *Opt. Mater. Express* **2020**, *10*, 1007–1017. [CrossRef]
37. Cao, Y.; Shao, Y.; Zhang, J.; Chen, C.; Wang, Q. The photothermal stability study of silica-coated $CsPbBr_3$ perovskite nanocrystals. *J. Solid State Chem.* **2022**, *311*, 123086. [CrossRef]
38. Zheng, Z.; Liu, L.; Yi, F.; Zhao, J. Significantly improving the moisture-, oxygen- and thermal-induced photoluminescence in all-inorganic halide perovskite $CsPbI_3$ crystals by coating the SiO_2 layer. *J. Lum.* **2019**, *216*, 116722. [CrossRef]
39. Tang, B.; Zhao, X.; Ruan, L.J.; Qin, C.; Shu, A.; Ma, Y. A universal synthesis strategy for stable $CsPbX_3$@oxide core–shell nanoparticles through bridging ligands. *Nanoscale* **2021**, *13*, 10600–10607. [CrossRef]
40. Liu, P.; Chen, W.; Wang, W.; Xu, B.; Wu, D.; Hao, J.; Cao, W.; Fang, F.; Li, Y.; Zeng, Y.; et al. Halide-Rich Synthesized Cesium Lead Bromide Perovskite Nanocrystals for Light-Emitting Diodes with Improved Performance. *Chem. Mater.* **2017**, *29*, 5168–5173. [CrossRef]
41. Liu, F.; Zhang, Y.; Ding, C.; Kobayashi, S.; Izuishi, T.; Nakazawa, N.; Toyoda, T.; Ohta, T.; Hayase, S.; Minemoto, T.; et al. Highly Luminescent Phase-Stable CsPbI3 Perovskite Quantum Dots Achieving Near 100% Absolute Photoluminescence Quantum Yield. *ACS Nano* **2017**, *11*, 10373–10383. [CrossRef]
42. Liu, H.; Xiao, X.; Wu, Y.; Zhu, D.; Sun, J.; Chen, D.; Tang, B.; Wang, S.; Portniagin, A.; Vighnesh, K.; et al. Pure-red electroluminescence of quantum-confined CsPbI3 perovskite nanocrystals obtained by the gradient purification method. *Mater. Taday Energy* **2024**, *41*, 101533. [CrossRef]
43. Pan, Z.; Zhu, X.; Xu, T.; Xie, Q.; Chen, H.; Xu, F.; Lin, H.; Wang, J.; Liu, Y. Highly Stable $CsPbI_3$ Perovskite Quantum Dots Enabled by Single SiO_2 Coating toward Down-Conversion Light-Emitting Diodes. *Appl. Sci.* **2023**, *13*, 7529. [CrossRef]
44. Miyata, K.; Meggiolaro, D.; Trinh, M.T.; Joshi, P.P.; Mosconi, E.; Jones, S.C.; De Angelis, F.; Zhu, X.Y. Large polarons in lead halide perovskites. *Sci. Mater.* **2017**, *3*, e1701217. [CrossRef] [PubMed]